47th AIAA/ASME/SAE/ASEE Joint Propulsion Conference & Exhibit
31 July - 03 August 2011, San Diego, California

AIAA 2011-5860

Viscous Flows Revisited in Simulated Rockets with Radially Regressing Walls

Tony Saad* and Joseph Majdalani†
University of Tennessee Space Institute, Tullahoma, TN 37388, USA

The mean gaseous motion in solid and, less commonly, hybrid rocket motors has been traditionally described assuming inviscid flow in a porous cylinder of fixed radius and constant mass addition at the sidewall. This model, usually referred to as the Taylor–Culick profile, is a simple inviscid rotational solution that captures the bulk gaseous motion in a rocket chamber with sidewall injection. In practice, however, the radius of the rocket motor increases as the propellant burns, thus leading to time-dependent effects on the mean flow that are not embraced by the Taylor–Culick model. In this work, we revisit the problem of the viscous flow in a porous cylinder and allow the radius to be time dependent. By implementing Uchida's well established similarity transformation in space and time, the incompressible Navier-Stokes equations are first reduced to a nonlinear fourth-order ordinary differential equation with four boundary conditions that contain, in the case of an axisymmetric chamber, an irregular limit. This equation is then solved both numerically and asymptotically, using the injection Reynolds number, Re, and the dimensionless wall regression ratio, α, as primary and secondary perturbation parameters. At the outset, closed-form analytical solutions are obtained for both large and small Re with small-to-moderate α. The resulting approximations are then compared to the numerical solution obtained for an equivalent third-order ODE in which both shooting and the irregular limit are circumvented. We find our code capable of producing the stable solutions for this problem over a wide range of Reynolds numbers and wall regression ratios. The code also enables us to confirm the accuracy of the asymptotic approximations, both of which being presented either for the first time in the case of small suction and injection or reconstructed with additional detail in the case of large injection.

Nomenclature

a	time dependent radius
$\dot{a}$	wall regression speed
F	mean flow function
r	radial coordinate
t	time
$\boldsymbol{u}$	velocity vector
z	axial coordinate

Greek

α	wall expansion ratio
ν	kinematic viscosity
ρ	density
$\boldsymbol{\Omega}$	vorticity vector
ψ	Stokes streamfunction

Subscripts

r, z	radial and axial component or partial derivative
θ	tangential component

Superscripts

$*$	dimensional variable

*Graduate Research Assistant, Mechanical, Aerospace and Biomedical Engineering Department. Presently Post Doctoral Fellow, Institute for Clean and Secure Energy, University of Utah. Member AIAA.
†H. H. Arnold Chair of Excellence in Advanced Propulsion and Professor, Mechanical, Aerospace and Biomedical Engineering Department. Associate Fellow AIAA. Fellow ASME.

I. Introduction

Viscous motion in cylindrical chambers with sidewall injection is of interest to a variety of applications including mean flow modeling of solid [1–3] and hybrid rockets, [4,5] sweat cooling, [6,7] boundary layer control, [8–10] peristaltic pumping, [11,12] gaseous diffusion, and isotope separation. [13–15] It is the latter group of studies by Berman [13,14] that has actually provided the impetus to develop the first similarity transformation of the Navier–Stokes equations into a fourth-order, nonlinear, ordinary differential equation (ODE). The resulting ODE was later solved asymptotically over different ranges of the wall injection Reynolds number. Most notable examples include those by Yuan and Finkelstein, [16] Terrill and Thomas, [17] Terrill, [18,19] Skalak and Wang, [20] and others.

In the propulsion area, an inviscid rotational counterpart known as the Taylor, [21] Culick, [22] or Taylor-Culick solution occupies the central stage in modeling the bulk gaseous motion inside solid rocket motors (SRMs). This may be owed to its association with several studies involving hydrodynamic instability, [23–28] acoustic instability, [29–35] wave propagation, [36–39] particle-mean flow interactions, [40] and rocket performance measurements. [41–43] The Taylor-Culick solution was originally verified to be an adequate representation of the expected flowfield in SRMs both numerically by Sabnis *et al.* [44] and, experimentally, by Dunlap *et al.*, [45,46] thusly confirming its character in a non-reactive chamber environment. It was extended by Majdalani and Akiki [4] to include effects of viscosity and headwall injection, by Saad *et al.* [42] and Sams *et al.* [43] to account for wall taper, by Kurdyumov [47] to capture effects of irregular cross sections, and by Majdalani and Saad [48] to allow for arbitrary headwall injection. Then using variational calculus and the Lagrangian optimization principle, Saad and Majdalani [49] uncovered a continuous spectrum of Taylor-like solutions exhibiting increasing kinetic energy signatures while ranging from the traditional Culick profile down to its predecessor, the irrotational mean flow known as the Hart-McClure profile. [50,51] This potential mean flow preceded the use of Culick's model in several fundamental investigations of combustion instability. [52–54] However, these studies have not been concerned with the time dependence that is inherent to the grain surface of a burning propellant.

In practical analysis, the radius of a rocket motor increases during wall regression, and the corresponding problem gives rise to a partial differential equation (PDE) in lieu of an ODE. While the problem in a tube with expanding or contracting surface was treated by Uchida and Aoki [12] in the late seventies, the effects of an injecting sidewall were incorporated more than a decade later, by Goto and Uchida [55] in the context of a pulsating porous tube and by Majdalani *et al.* [1,2] in the context of a rocket chamber. In their work, the effect of wall regression was prescribed by a dimensionless wall expansion ratio, α, written as a viscous Reynolds number based on the radial regression speed of the sidewall. In the interim, Dauenhauer and Majdalani [56–58] formulated the corresponding equation and numerical solution for the planar flow analog. The analytical solutions promoted through these efforts would later receive attention in follow-up studies aimed at devising asymptotic approximations over various ranges of the control parameters, or at reconstructing the solution using alternative techniques such as the Lie-group theory [59,60] or the Homotopy-Analysis Method. [61–63]

In this article, we revisit the problem of viscous motion in a porous cylinder and allow the radius to transiently expand or contract. [1,2] As before, we employ a dual similarity transformation in space and time to reduce the Navier-Stokes equations into a nonlinear, fourth-order ODE that can be solved both asymptotically and numerically. After reconstructing the analytical solution of Majdalani *et al.* [1,2] for large injection, we employ two perturbation parameters, the injection Reynolds number, Re, and the wall expansion ratio, α, to formulate an asymptotic series for the case of small Re and small-to-moderate α. We then introduce an efficient numerical approach that overcomes the singularity encountered in this model, specifically in the form of an intrinsically satisfied limit at the origin. To make headway, an equivalent third-order ODE is presented and solved using a technique that may be attributed to Terrill and Thomas. [17] Subsequent numerical predictions are obtained directly, with no shooting or iteration, and then compared to our analytical approximations. In this manner, the robustness of the numerical algorithm is used to demonstrate that the present approach can capture the stable solutions for this problem over a wide range of Re and α.

The paper is organized as follows. First, we consider the mathematical model developed by Majdalani *et al.* [1,2] and reaffirm its validity. Second, we discuss the numerical technique that appears to be most practical. Third, we produce regular perturbation approximations for the large and small injection cases, the latter of which being presented for the first time. Finally, we compare asymptotics and numerics over a practical range of the control parameters.

II. Mathematical Model

The cylindrical propellant grain of a solid rocket motor is modeled as a long tube with one end closed at the headwall, and the other end open. The circumference of the wall is assumed to be permeable so as to simulate

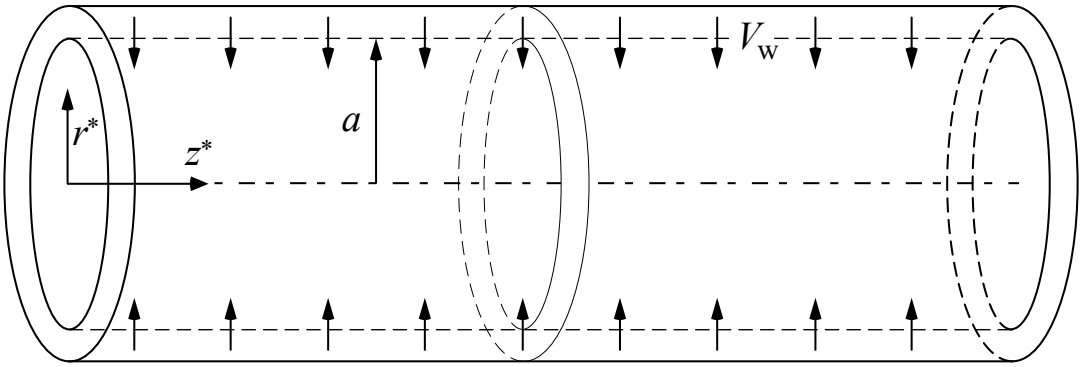

Figure 1. Schematic of a cylindrical chamber used to illustrate sidewall injection and wall regression as well as the control volume used to evaluate the average axial velocity.

propellant burning and normal gas injection. Furthermore, the wet area of the cylinder is allowed to radially expand at a speed equal to $\dot{a}$. For this to occur, the mathematical model requires that the headwall area stretches accordingly to accommodate the expansion of the cylinder. This behavior is shown in Fig. 1 where an axisymmetric coordinate system is defined. By assuming an incompressible mean flow, the vorticity transport equation is written as

$$\frac{\partial \boldsymbol{\Omega}^*}{\partial t} - \nabla^* \times (\boldsymbol{u}^* \times \boldsymbol{\Omega}^*) = \nu \nabla^* \times \nabla^{*2} \boldsymbol{u}^* \tag{1}$$

A. Boundary Conditions

These can be organized as follows

$$r^* = a(t) : \begin{cases} u_r^* = -V & \text{sidewall injection} \\ u_z^* = 0 & \text{no slip} \end{cases} \tag{2}$$

$$r^* = 0 : \begin{cases} u_r^* = 0 & \text{no flow across the centerline} \\ \dfrac{\partial u_z^*}{\partial r^*} = 0 & \text{axial velocity symmetry} \end{cases} \tag{3}$$

$$z^* = 0 : \quad u_z^* = 0 \quad \text{inert headwall} \tag{4}$$

Here, V is the absolute fluid injection velocity at the wall. It is defined as the fluid velocity seen by an observer in a reference frame located outside of the cylinder. If V_w is used to denote the fluid velocity with respect to the wall, then we have the following relation

$$V = V_w - \dot{a} \tag{5}$$

Evidently, when the walls are stationary, the absolute and relative velocities become equal. But when the wall undergoes inward contraction, then $\dot{a} < 0$ and the fluid will appear as if it is being injected at a larger speed than V_w. Conversely, if the the wall regresses outwardly, then $\dot{a} > 0$ and the fluid injection velocity will appear to be smaller than V_w.

B. Similarity in Space

By inspection, one expects the axial velocity to vary linearly in z^*. To show this, we follow Majdalani and coworkers [1–3] by considering the control volume delineated by the dashed lines in Fig. 1. Through a mass balance on the inlet and outlet surfaces, we superimpose

$$\frac{\partial}{\partial t} \int_{\mathcal{V}} \rho \, \mathrm{d}\mathcal{V} + \iint_{\mathcal{S}} \rho \boldsymbol{u}^* \cdot \boldsymbol{n} \, \mathrm{d}\mathcal{S} = 0 \tag{6}$$

or

$$\frac{\partial \mathcal{V}}{\partial t} + \iint_{\mathcal{S}_{\text{exit}}} \boldsymbol{u}^* \cdot \boldsymbol{n}\, \mathrm{d}\mathcal{S} + \iint_{\mathcal{S}_{\text{sidewall}}} \boldsymbol{u}^* \cdot \boldsymbol{n}\, \mathrm{d}\mathcal{S} = 0 \tag{7}$$

This yields

$$\frac{\partial \mathcal{V}}{\partial t} + \iint_{\mathcal{S}_{\text{exit}}} \boldsymbol{u}^* \cdot \boldsymbol{n}\, \mathrm{d}\mathcal{S} - 2\pi V a z^* = 0 \tag{8}$$

The second integral in Eq. (8) is related to the average axial velocity U_{m} inside the volume via

$$U_{\text{m}} = \frac{1}{\pi a^2} \iint_{\mathcal{S}_{\text{exit}}} \boldsymbol{u}^* \cdot \boldsymbol{n}\, \mathrm{d}\mathcal{S} \tag{9}$$

Its substitution into Eq. (8) gives

$$\frac{\partial \mathcal{V}}{\partial t} + \pi a^2 U_{\text{m}} - 2\pi V a z^* = 0 \tag{10}$$

and so, by using $\mathcal{V} = \pi a^2 z^*$, Eq. (10) reduces to

$$2\pi a \dot{a} z^* + \pi a^2 U_{\text{m}} - 2\pi V a z^* = 0 \tag{11}$$

Thus, based on mass conservation alone, we must have

$$U_{\text{m}} = 2V \frac{z^*}{a} \tag{12}$$

which must be equated to the areal integral for the average velocity,

$$U_{\text{m}}(z^*, t) = \frac{1}{\pi a^2} \int_0^a u_z^*(r^*, z^*, t) r^*\, \mathrm{d}r^* = 2V \frac{z^*}{a} \tag{13}$$

This proves that the only admissible form of the axial velocity is a linear relation of the type:

$$u_z^*(r^*, z^*, t) = z^* f(r^*, t) \tag{14}$$

C. Vorticity Transport Equation

We introduce the Stokes streamfunction via

$$u_r^* = -\frac{1}{r^*} \frac{\partial \psi^*}{\partial z^*}; \quad u_z^* = \frac{1}{r^*} \frac{\partial \psi^*}{\partial r^*} \tag{15}$$

Based on Eq. (14), the streamfunction may be written as

$$\psi^* = \nu z^* F(r, t); \quad r = \frac{r^*}{a} \tag{16}$$

where ν is the kinematic viscosity. Note that $F(r, t)$ is dimensionless. The radial and axial velocities can now be expressed in terms of F. This operation yields

$$u_r^* = -\frac{\nu}{ar} F, \quad u_z^* = \frac{\nu z^*}{a^2 r} \frac{\partial F}{\partial r} \tag{17}$$

Since u_r^* remains independent of the axial coordinate, the vorticity displays a single nonzero component in the tangential direction viz.

$$\Omega^* = \Omega_\theta^* = \frac{\partial u_r^*}{\partial z^*} - \frac{\partial u_z^*}{\partial r^*} = -\frac{\partial u_z^*}{\partial r^*} \tag{18}$$

Upon substitution of Eq. (18) into Eq. (1), one recovers

$$\frac{\partial}{\partial r^*}\left(\frac{\partial u_z^*}{\partial t}\right) + \frac{\partial}{\partial r^*}\left(u_r^* \frac{\partial u_z^*}{\partial r^*}\right) + \frac{\partial}{\partial r^*}\left(u_z^* \frac{\partial u_z^*}{\partial z^*}\right) - \nu \frac{\partial}{\partial r^*}\left[\frac{1}{r^*} \frac{\partial}{\partial r^*}\left(r^* \frac{\partial u_z^*}{\partial r^*}\right)\right] = 0 \tag{19}$$

where we have used

$$\frac{\partial}{\partial z^*}\left(u_z^*\frac{\partial u_z^*}{\partial r^*}\right) = \frac{\partial}{\partial r^*}\left(u_z^*\frac{\partial u_z^*}{\partial z^*}\right) \tag{20}$$

We now evaluate every term in Eq. (19), paying particular attention to partial differentiation:

$$\frac{\partial u_z^*}{\partial t} = \frac{\nu z^*}{a^2}\left(\frac{F_r}{r}\right)_t - \frac{2\nu z^*}{a^3}\frac{F_r}{r}\dot{a} \tag{21a}$$

$$\frac{\partial u_z^*}{\partial r^*} = \frac{\nu z^*}{a^3}\left(\frac{F_r}{r}\right)_r \tag{21b}$$

$$\frac{u_z^*}{z^*} = \frac{\nu}{a^2}\frac{F_r}{r} \tag{21c}$$

$$u_r^*\frac{\partial u_z^*}{\partial r^*} = -\frac{\nu^2 z^*}{a^4}\frac{F}{r}\left(\frac{F_r}{r}\right)_r \tag{21d}$$

$$u_z^*\frac{\partial u_z^*}{\partial z^*} = \frac{\nu^2 z^*}{a^4}\left(\frac{F_r}{r}\right)^2 \tag{21e}$$

$$\frac{1}{r^*}\frac{\partial}{\partial r^*}\left(r^*\frac{\partial u_z^*}{\partial r^*}\right) = \frac{\nu z^*}{a^4 r}\frac{\partial}{\partial r}\left[r\left(\frac{F_r}{r}\right)_r\right] \tag{21f}$$

For example, evaluation of the time derivative in Eq. (21a) is carried out in several steps such as:

$$\left(\frac{F_r}{r}\right)_t = \frac{\mathrm{d}r^{-1}}{\mathrm{d}t}F_r + \frac{1}{r}\frac{\mathrm{d}F_r}{\mathrm{d}t} \tag{22}$$

or

$$\begin{cases} \dfrac{\mathrm{d}r}{\mathrm{d}t} = \dfrac{\mathrm{d}\left[r^*/a(t)\right]}{\mathrm{d}t} = -r^*\dfrac{\dot{a}}{a^2} = -\dfrac{\dot{a}}{a}r \\ \dfrac{\mathrm{d}}{\mathrm{d}t}\left(\dfrac{1}{r}\right) = \dfrac{\partial}{\partial r}\left(\dfrac{1}{r}\right)\dfrac{\mathrm{d}r}{\mathrm{d}t} + \underbrace{\dfrac{\partial}{\partial t}\left(\dfrac{1}{r}\right)}_{0} = \dfrac{\dot{a}}{ar} \\ \dfrac{\mathrm{d}F_r}{\mathrm{d}t} = \dfrac{\partial F_r}{\partial r}\dfrac{\mathrm{d}r}{\mathrm{d}t} + \dfrac{\partial F_r}{\partial t} = -\dfrac{\dot{a}}{a}rF_{rr} + F_{rt} \end{cases} \tag{23}$$

Upon substitution and collection of terms, we recover

$$\left\{-\frac{a^2}{\nu}\frac{F_{rt}}{r} + \frac{a\dot{a}}{\nu}r\left(\frac{F_r}{r}\right)_r + 2\frac{a\dot{a}}{\nu}\frac{F_r}{r} + \frac{F}{r}\left(\frac{F_r}{r}\right)_r - \left(\frac{F_r}{r}\right)^2 + \frac{1}{r}\left(\frac{F_r}{r}\right)_r\left(\frac{F_r}{r}\right)_{rr}\right\}_r = 0 \tag{24}$$

Thus, if we define the wall expansion ratio

$$\alpha(t) \equiv \frac{a\dot{a}}{\nu} \tag{25}$$

then Eq. (24) becomes

$$\left\{\left(\frac{F_r}{r}\right)_{rr} + \left(\frac{1}{r} + \frac{F}{r} + \alpha r\right)\left(\frac{F_r}{r}\right)_r - \left(\frac{F_r}{r} - 2\alpha\right)\frac{F_r}{r} - \frac{a^2}{\nu}\frac{F_{rt}}{r}\right\}_r = 0 \tag{26}$$

This can be integrated with respect to r and rearranged as

$$\left(\frac{F_r}{r}\right)_{rr} + \left(\frac{1}{r} + \frac{F}{r} + \alpha r\right)\left(\frac{F_r}{r}\right)_r - \left(\frac{F_r}{r} - 2\alpha\right)\frac{F_r}{r} - \frac{a^2}{\nu}\frac{F_{rt}}{r} = K \tag{27}$$

The formidable PDE that we arrive at embodies the physics of viscous motion in a porous pipe with regressing walls. It is related to work by Uchida and Aoki[12] who studied a similar problem in the context of pipe flow with expanding

or contracting impermeable walls. Goto and Uchida,[55] Dauenhauer and Majdalani,[56–58] and Majdalani *et al.*[1,2] later extended Uchida's problem to allow fluid injection or suction along the moving sidewall. Their analysis was carried out for both planar and cylindrical configurations. Majdalani and coworkers[1–3] also derived asymptotic solutions for this equation over a practical range of Reynolds numbers and expansion ratios.

D. Similarity in Time

At first glance, Eq. (27) may seem intractable using any of the standard analytical techniques. This excludes the Homotopy Analysis Method which has been shown recently to handle highly nonlinear equations quite admirably.[61,64–66] By utilizing a practical hypothesis that may be traced back to Uchida,[12] Eq. (27) may be reduced to a third-order nonlinear ODE. As shown by Majdalani *et al.*,[1] this is accomplished by setting

$$\alpha(t) = \text{constant}; \quad F(r,t) \mapsto F[r, \alpha(t)] \tag{28}$$

The constancy of α ensures that

$$F_{rt} = \frac{\partial F_r}{\partial \alpha}\frac{\mathrm{d}\alpha}{\mathrm{d}t} = 0 \tag{29}$$

One can then deduce the required wall regression speed for which α becomes a constant. According to this model

$$\alpha = \frac{a\dot{a}}{\nu} = \frac{a_0\dot{a}_0}{\nu} \tag{30}$$

where a_0 and $\dot{a}_0$ correspond to the initial radius and regression speed, respectively. Upon integration, we get

$$a(t) = a_0\sqrt{1 + 2\frac{\nu\alpha}{a_0^2}t} \tag{31}$$

Note that this model does not suppress time dependence, but rather embeds it within the solution implicitly. This is realized by specifying the regression speed in such a way that $\alpha(t)$ remains a constant.

Before substituting the time similarity conditions into Eq. (27), we find it useful to introduce the following normalizations

$$F \mapsto \frac{F}{Re}; \quad \eta \equiv \tfrac{1}{2}r^2 \tag{32}$$

where Re is the sidewall injection Reynolds number based on the absolute velocity of the fluid,

$$Re \equiv \frac{Va}{\nu} = \frac{V_w a}{\nu} - \alpha \tag{33}$$

In this setting, the Reynolds number remains a function of time. To make further headway, we assume that Re = constant, or

$$\frac{V_w a}{\nu} = \frac{V_{w0}a_0}{\nu} \tag{34}$$

This requirement enables us to extract the proper form of V_w in our model, namely

$$V_w = \frac{V_{w0}a_0}{a} = V_{w0}\left(1 + 2\frac{\nu\alpha}{a_0^2}t\right)^{-\frac{1}{2}} \tag{35}$$

Finally, backward substitution of Eq. (32) into Eq. (27) yields

$$\eta F''' + F'' + \tfrac{1}{2}Re(FF'' - F'^2) + \alpha(\eta F'' + F') = K(Re) \tag{36}$$

where primes denote differentiation with respect to η. To eliminate the constant $K(Re)$, one differentiates Eq. (36) with respect to η and writes

$$\eta F'''' + \alpha(\eta F''' + 2F'') + \tfrac{1}{2}Re(FF''' - F'F'') + 2F''' = 0 \tag{37}$$

Finally, the boundary conditions may be assimilated into the following set

$$\frac{\mathrm{d}F(\frac{1}{2})}{\mathrm{d}\eta} = 0 \tag{38a}$$

$$F(\tfrac{1}{2}) = 1 \tag{38b}$$

$$F(0) = 0 \tag{38c}$$

$$\lim_{\eta\to 0} \sqrt{2\eta}\frac{\mathrm{d}^2F}{\mathrm{d}\eta^2} = 0 \tag{38d}$$

Note that the constant $K(Re)$ may be specified by evaluating Eq. (36) at any location inside the domain such as the centerline. At $r = 0$, one gets

$$K(Re) = F''(0) + \tfrac{1}{2}ReF'^2(0) + \alpha F'(0) \tag{39}$$

Either of the differential equations given by Eqs. (36–37) may be used to solve for the mean flow function $F(\eta)$. The choice depends on the type of solution sought. For example, we elect to use Eq. (36) for the numerical solution because it requires less memory storage and fewer Runge–Kutta integrations. On the other hand, Eq. (37) will be used to initiate the regular perturbation expansion because of the implicit nonlinearity that the constant $K(Re)$ embodies.

III. Numerical Technique

Being nonlinear ODEs, Eqs. (36–37) may be solved directly through a Runge–Kutta integration routine. However, a close inspection of the boundary conditions as well as the governing equations reveals several difficulties. Firstly, the explicit presence of η in either equation requires a careful treatment by virtue of the singularity at the origin. This matter may be settled through a Taylor series expansion near the centerline. Secondly, the boundary conditions given by Eq. (38) result in a boundary value problem that requires a double infinity of integrations.[17] While this problem may be overcome via a shooting method based on a Newton-Raphson root finding algorithm such as the one proposed by Dauenhauer and Majdalani;[58] however, the fourth boundary condition in Eq. (38d) will add an undesirable complication. The reason is that, as long as $F''(0)$ remains finite, Eq. (38d) will be intrinsically satisfied. Indeed, one expects $F''(0)$ to be finite as it corresponds to the vorticity at the centerline. In short, we find Eq. (38d) to be impractical for numerical treatment.

The above-mentioned issues may be overcome if one uses a transformation that is nearly identical to that employed by Terrill and Thomas[17] who encounter similar difficulty in a problem involving flow through a porous cylinder. In our model, however, one needs to incorporate the effect of α. By allowing both the Reynolds number Re and α to be determined a posteriori, i.e. at the end of integration, a shooting method will no longer be required and the numerical solution may be arrived at directly, using a single Runge–Kutta integration. To illustrate this procedure, we begin by introducing the dual transformation

$$F = \lambda G(\xi); \quad \xi = b\,\eta \tag{40}$$

where both λ and b are scaling factors that will be determined once the numerical integration is complete. Upon substitution into Eq. (36) , we recover a third-order ODE in $G(\xi)$, namely,

$$\xi G''' + G'' + \tfrac{1}{2}\lambda Re(GG'' - G'^2) + \frac{\alpha}{b}(\xi G'' + G') = \frac{K}{\lambda b^2} = K_1 \tag{41}$$

where the primes denote differentiation with respect to ξ. If we further set

$$\lambda = \frac{2}{Re} \quad \text{and} \quad \beta = \frac{\alpha}{b} \tag{42}$$

then Eq. (41) reduces to the convenient form,

$$\xi G''' + G'' + GG'' - G'^2 + \beta(\xi G'' + G') = K_1 \tag{43}$$

Algorithm 1: RK4INTEGRATE()

allocate memory for arrays
process user input: $G(0)$, $G'(0)$, $G''(0)$, β, $n_{\max}$, n_{Taylor}, $\xi_{\max}$
calculate K_1
calculate Taylor series coefficients γ_i
for $i \leftarrow 0$ **to** n_{Taylor}
  do calculate $G(\xi)$ near the centerline
for $i \leftarrow n_{\text{Taylor}}$ **to** $n_{\max}$
  do integrate governing equation
for $i \leftarrow 0$ **to** $n_{\max}$
  do find $n_p \setminus G'(n_p) = 0$
calculate ξ_p that corresponds to n_p
$\xi_{\max} \leftarrow \xi_p + \epsilon$
for $i \leftarrow n_{\text{Taylor}}$ **to** $n_{\max}$
  do integrate governing equation using
for $i \leftarrow 0$ **to** $n_{\max}$
  do find $n_p \setminus G'(n_p) = 0$
calculate ξ_p that corresponds to n_p
$b \leftarrow 2\xi_p$
$\alpha \leftarrow b\beta$
$Re \leftarrow 2G(n_p)$

Algorithm 1. Here, $\xi_{\max}$ is the interval size (starting from zero), $n_{\max}$ is the number of points that divides the interval, and n_{Taylor} is the number of points for which the Taylor series expansion is to be applied. Note that n_p corresponds to the point where $G'(n_p) = 0$ and ϵ is a small number. All subscripts with p correspond to this particular point.

Finally, by applying this procedure to the conditions encapsulated in Eq. (38), they transform to

$$\frac{\mathrm{d}G(\frac{1}{2}b)}{\mathrm{d}\xi} = 0 \tag{44a}$$

$$G(\tfrac{1}{2}b) = \frac{1}{\lambda} = \frac{Re}{2} \tag{44b}$$

$$G(0) = 0 \tag{44c}$$

$$\lim_{\xi \to 0} \sqrt{\xi} \frac{\mathrm{d}^2 G}{\mathrm{d}\xi^2} = 0 \tag{44d}$$

By initializing the solution with arbitrary values for $G'(0)$, $G''(0)$, and β, the integration is carried out until $G'(\frac{1}{2}b) = 0$. The point at which G' vanishes enables us to explicitly deduce b with no need for iteration. Subsequently, the Reynolds number and α may be calculated from Eq. (44b) as $Re = 2G(\frac{1}{2}b)$ and $\alpha = \beta b$. The constant K_1 can also be extracted from the initial guesses by putting

$$K_1 = G''(0) - G'(0)^2 + \beta G'(0) \tag{45}$$

Finally, near centerline ($\xi \to 0$), a Taylor series expansion of the governing equation is required. Using

$$G(\xi) = \sum_{i=0} \gamma_i \xi^i \tag{46}$$

substitution into Eq. (43) yields

$$\gamma_0 = G(0) = 0; \quad \gamma_1 = G'(0); \quad \gamma_2 = \tfrac{1}{2}G''(0) \tag{47}$$

Note that these coefficients are known since the values of the first and second derivatives at the centerline are used to seed the numerical solution. Then, by substituting Eq. (46) into Eq. (36), coefficients of the same order may be equated to the extent of establishing a recurrence formula for the coefficients of the Taylor series expansion; we get

$$\begin{aligned}(n+2)(n+1)^2\gamma_{n+2} = &\sum_{j=0}^{n}(j+1)(n-j+1)\gamma_{j+1}\gamma_{n-j+1} - \sum_{j=0}^{n}(j+1)(j+2)\gamma_{j+2}\gamma_{n-j} \\ &-\beta(n+1)^2\gamma_{n+1}; \quad n \geq 1\end{aligned} \tag{48}$$

Algorithm 1 lists the necessary steps for our numerical implementation. Results of the numerical simulation will be presented in subsequent sections where they will be compared to the asymptotic approximations.

IV. Asymptotic Treatment

A. Large Injection

In this case, which is appropriate for modeling gaseous injection in solid rocket motors, the Reynolds number is sufficiently large to warrant a regular perturbation in the inverse of the Reynolds number. We follow Majdalani *et al.* [1] and write

$$F = F_0 + \varepsilon F_1 + O(\varepsilon^2); \quad \varepsilon \equiv \frac{1}{Re} \tag{49}$$

Upon substitution into Eq. (37), we recover the ODEs for the leading and first-order solutions. These are

$$O(0): \quad F_0F_0''' - F_0'F_0'' = 0 \tag{50a}$$

$$O(1): \quad F_0F_1''' + F_1F_0''' - F_0'F_1'' - F_1'F_0'' + 2\eta F_0'''' + (2\alpha\eta + 4)F_0''' + 4\alpha F_0'' = 0 \tag{50b}$$

Note that we limit our analysis to the leading and first-order approximations partly due to the excellent agreement that we later show between the present solution and numerical simulations.

1. Leading-Order Solution

At leading order, we have

$$F_0F_0''' - F_0'F_0'' = 0 \tag{51}$$

This can be solved by inspection to obtain

$$F_0 = \sin(\pi\eta) = \sin\theta; \quad \theta = \pi\eta \tag{52}$$

Equation (52) corresponds to the Taylor–Culick mean flow with no wall regression. [22]

2. First-Order Solution

By substituting Eq. (52) into Eq. (50b), the ODE for the first-order term may be determined,

$$\begin{aligned}\sin\theta F_1''' - \cos\theta F_1 - \cos\theta F_1'' + \sin\theta F_1' = \\ -2\vartheta\sin\theta + (2\pi^{-1}\alpha\theta + 4)\cos\theta + 4\pi^{-1}\alpha\sin\theta\end{aligned} \tag{53}$$

The solution of Eq. (53) requires the identification of a homogeneous solution. This can be obtained by solving

$$\sin\theta F_{1h}''' - \cos\theta F_{1h} - \cos\theta F_{1h}'' + \sin\theta F_{1h}' = 0 \tag{54}$$

for which a particular form may be noted to be

$$F_{1h} = C\cos\theta \tag{55}$$

To determine a more general homogeneous solution, we allow the constant in Eq. (55) to be a function of θ by setting

$$F_{1h} = C(\theta)\cos\theta \tag{56}$$

Upon substitution of Eq. (56) into Eq. (54), one obtains the differential equation governing $C(\theta)$, namely,

$$C'''\sin\theta\cos\theta - 2C''\sin^2\theta - C'' = 0 \tag{57}$$

The solution of Eq. (57) may be managed through division by $C''\sin\theta\cos\theta$ before integration. This operation yields

$$C(\theta) = \tfrac{1}{2}K_0\tan\theta + K_1\theta + K_2 \tag{58}$$

Finally, the general homogeneous solution of Eq. (54) emerges as

$$F_{1h} = C(\theta)\cos\theta = K_0\sin\theta + K_1\theta\cos\theta + K_2\cos\theta \tag{59}$$

To obtain the total solution for Eq. (53), we use variation of parameters and rewrite

$$F_1 = K_0(\theta)\sin\theta + K_1(\theta)\theta\cos\theta + K_2(\theta)\cos\theta \tag{60}$$

then, upon differentiation, we get

$$F_1' = K_0\cos\theta + K_1(\cos\theta - \theta\sin\theta) - K_2\sin\theta \tag{61a}$$
$$F_1'' = -K_0\sin\theta + K_1(-2\sin\theta - \theta\cos\theta) - K_2\cos\theta \tag{61b}$$
$$F_1''' = -2K_1'\sin\theta - K_0\cos\theta + K_1(-2\cos\theta - \cos\theta + \theta\sin\theta) + K_2\sin\theta \tag{61c}$$

along with the auxiliary conditions

$$K_0'\sin\theta + K_1'\theta\cos\theta + K_2'\cos\theta = 0 \tag{62a}$$
$$K_0'\cos\theta + K_1'(\cos\theta - \theta\sin\theta) - K_2'\sin\theta = 0 \tag{62b}$$

Inserting Eq. (61) into Eq. (53) leads to

$$-2K_1'\sin^2\theta = (2\pi^{-1}\alpha\theta + 4)\cos\theta + 4\pi^{-1}\alpha\sin\theta - 2\theta\sin\theta \tag{63}$$

which can be divided by $\sin\theta$ so that

$$-2K_1'\sin\theta = (2\pi^{-1}\alpha\theta + 4)\cot\theta + 4\pi^{-1}\alpha - 2\theta \tag{64}$$

At this juncture, one can solve Eq. (64) in conjunction with Eq. (62) simultaneously for K_0', K_1', and K_2'. The resulting system may be conveniently written in matrix form,

$$\begin{bmatrix} \sin\theta & \theta\cos\theta & \cos\theta \\ \cos\theta & \cos\theta - \theta\sin\theta & -\sin\theta \\ 0 & -2\sin\theta & 0 \end{bmatrix}\begin{bmatrix} K_0' \\ K_1' \\ K_2' \end{bmatrix} = \begin{bmatrix} 0 \\ 0 \\ (\frac{2}{\pi}\alpha\theta + 4)\cot\theta + \frac{4}{\pi}\alpha - 2\theta \end{bmatrix} \tag{65}$$

Upon inversion, one recovers the differential equations for K_0', K_1', and K_2'

$$K_0' = -\theta\cos\theta\cot\theta + \frac{2}{\pi}\alpha\cos\theta\cot\theta + 2\cos\theta\cot^2\theta + \frac{\alpha}{\pi}\theta\cos\theta\cot^2\theta \tag{66}$$

$$K_1' = \theta\csc\theta - \frac{2}{\pi}\alpha\csc\theta - 2\cot\theta\csc\theta - \frac{\alpha}{\pi}\theta\cot\theta\csc\theta \tag{67}$$

$$\begin{aligned} K_2' = -\frac{2}{\pi}\alpha\cos\theta + \frac{2}{\pi}\alpha\theta\csc\theta + \theta\cos\theta - \theta^2\csc\theta - 2\cot\theta\cos\theta \\ +2\theta\cot\theta\csc\theta - \frac{\alpha}{\pi}\theta\cos\theta\cot\theta + \frac{\alpha}{\pi}\theta^2\cot\theta\csc\theta \end{aligned} \tag{68}$$

This can be further integrated to give

$$K_0 = \frac{\alpha}{\pi}\left(\cos\theta + 3\ln\tan\tfrac{1}{2}\theta - \theta\sin\theta - \theta\csc\theta\right) - \theta\cos\theta - \sin\theta \\ - 2\csc\theta - S(\theta) + C_0 \tag{69}$$

$$K_1 = \frac{\alpha}{\pi}\left(\theta\csc\theta - 3\ln\tan\tfrac{1}{2}\theta\right) + 2\csc\theta + S(\theta) + C_1 \tag{70}$$

$$K_2 = \frac{\alpha}{\pi}\left[3S(\theta) - \sin\theta - \theta^2\csc\theta - \theta\cos\theta\right] - \cos\theta + \theta\sin\theta - 2\theta\csc\theta - S_1(\theta) + C_2 \tag{71}$$

where

$$S(\theta) = \int_0^\theta \phi\csc\phi\,\mathrm{d}\phi; \quad S_1(\theta) = \int_0^\theta \phi^2\csc\phi\,\mathrm{d}\phi \tag{72}$$

and C_0, C_1, and C_2 are constants that can be determined by invoking the boundary conditions in Eq. (38). The first-order solution given by Eq. (60) is now at hand, specifically

$$F_1 = \frac{\alpha}{\pi}\left[3\ln\tan\tfrac{1}{2}\theta(\sin\theta - \theta\cos\theta) - 2\theta\right] + \frac{3}{\pi}\alpha\cos\theta S(\theta) - 3 - S_1(\theta)\cos\theta \\ + (\theta\cos\theta - \sin\theta)S(\theta) + C_0\sin\theta + C_1\theta\cos\theta + C_2\cos\theta \tag{73}$$

What is left is the application of the boundary conditions, and these require that

$$F_1(\tfrac{1}{2}\pi) = 0 \quad \text{or} \quad C_0 = 3 + \alpha + S(\tfrac{1}{2}\pi) \tag{74}$$

in conjunction with

$$\lim_{\theta\to 0} F_1(\theta) = 0; \quad \text{or} \quad C_2 = 3 \tag{75}$$

and finally

$$\frac{\mathrm{d}F_1\left(\frac{1}{2}\right)}{\mathrm{d}\eta} = \pi\frac{\mathrm{d}F_1\left(\frac{1}{2}\pi\right)}{\mathrm{d}\theta} = 0 \tag{76}$$

from which we extract

$$C_1 = -1 - \frac{6}{\pi} + \frac{2}{\pi^2}\alpha + \frac{2}{\pi}S_1(\tfrac{1}{2}\pi) - S(\tfrac{1}{2}\pi)\left(\frac{6}{\pi^2}\alpha + 1\right) \tag{77}$$

3. Verification

The total solution may now be assembled into

$$F = F_0 + \varepsilon F_1 + O(\varepsilon^2) = \sin\theta + \varepsilon\left\{\frac{\alpha}{\pi}\left[3\ln(\tan\tfrac{1}{2}\theta)(\sin\theta - \theta\cos\theta) - 2\theta\right]\right. \\ + \frac{3}{\pi}\alpha\cos\theta\, S(\theta) - 3 - S_1(\theta)\cos\theta + (\theta\cos\theta - \sin\theta)S(\theta) \\ \left. + C_0\sin\theta + C_1\theta\cos\theta + C_2\cos\theta\right\} + O(\varepsilon^2) \tag{78}$$

This result is identical to the one obtained by Majdalani *et al.*[1,2] where corresponding flow attributes such as velocity, pressure, and vorticity are described. In this study, we limit ourselves to the detailed mathematical derivation and verification using a robust numerical solution. To this end, Eq. (78) is compared to results from the Runge–Kutta integration for Reynolds numbers of 100, 500, and 1000 taken at different values of the wall expansion ratio, namely, at $\alpha = 10$, 20, -10, and -20.

Starting with the mean flow function F, corresponding graphs are shown in Figs. 2–3. The first noticeable feature is the accuracy of the solution for large Re regardless of the wall expansion ratio. In fact, even for the relatively small value of $Re = 100$, the curves are visually indistinguishable unless one uses magnification on certain areas of the graphs. The other noteworthy feature is the effect of decreasing the wall expansion ratio. Specifically, the curves become increasingly more difficult to discern apart as one scans the plots sequentially starting with the largest value of α in Figs. 2b–3b.

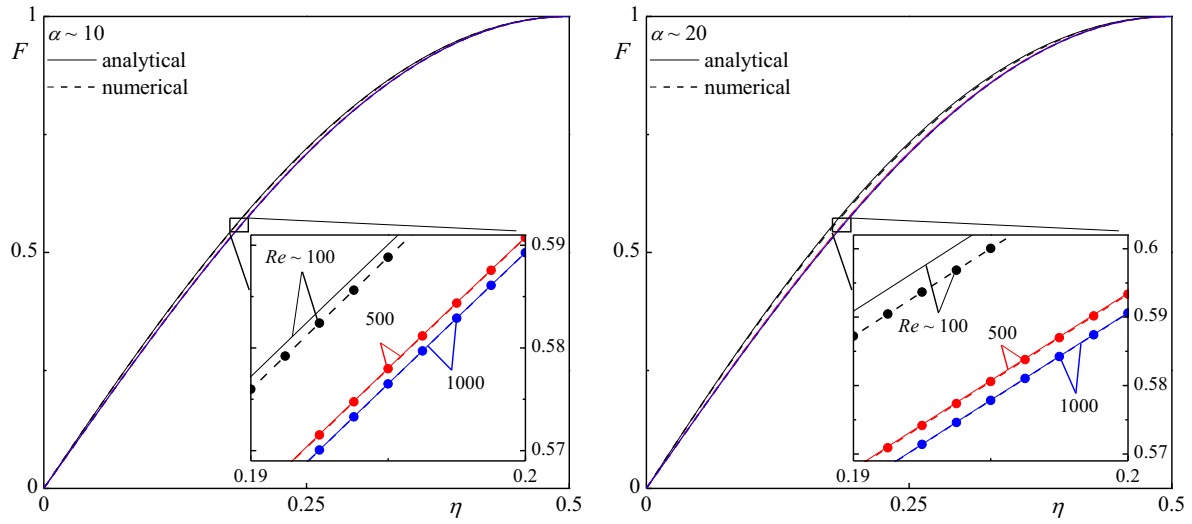

a) $\alpha \approx 10$ **b)** $\alpha \approx 20$

Figure 2. Comparison between analytical (—) and numerical solutions (○) for the mean flow function F using a) $\alpha \approx 10$, and b) $\alpha \approx 20$. Curves are shown for $Re \approx 100$, 500, and 1000. Everywhere, inset frames are used for added magnification and clarity.

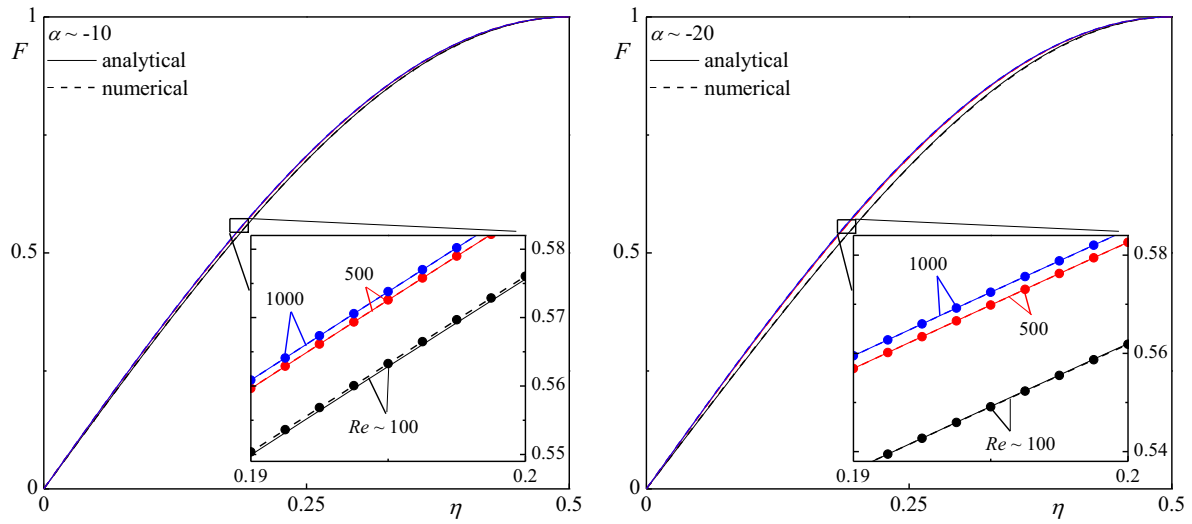

a) $\alpha \approx -10$ **b)** $\alpha \approx -20$

Figure 3. Comparison between analytical (—) and numerical solutions (○) for the mean flow function F using a) $\alpha \approx -10$, and b) $\alpha \approx -20$. Curves are shown for $Re \approx 100$, 500, and 1000.

The second set of comparisons is provided in Figs. 4–5 for F'. We recall that the derivative of the mean flow function is directly connected to the axial velocity and, as such, the importance of arriving at a reliable analytical representation for $F'(\eta)$ cannot be underrated. In this case, similar trends are observed as those corresponding to F. The most prominent feature in these graphs is the effect of α on the centerline velocity. As the wall expansion ratio is decreased so does the centerline velocity. Altogether, the curves are practically inseparable, a satisfactory observation given that our solution is of first-order accuracy.

Additional confirmatory comparisons between numerics and asymptotics are provided in Tables 1 and 2 where F, F' and F'' are listed side-by-side with their numerical predictions for three injection Reynolds numbers of 100, 500 and 1000, and either $\alpha = 10$ (Table 1) or -10 (Table 2). Calculated values are given at five characteristic radial positions corresponding to $\eta = 0, 0.125, 0.25, 0.375$ and 0.5. Irrespective of whether the injecting surface is expanding

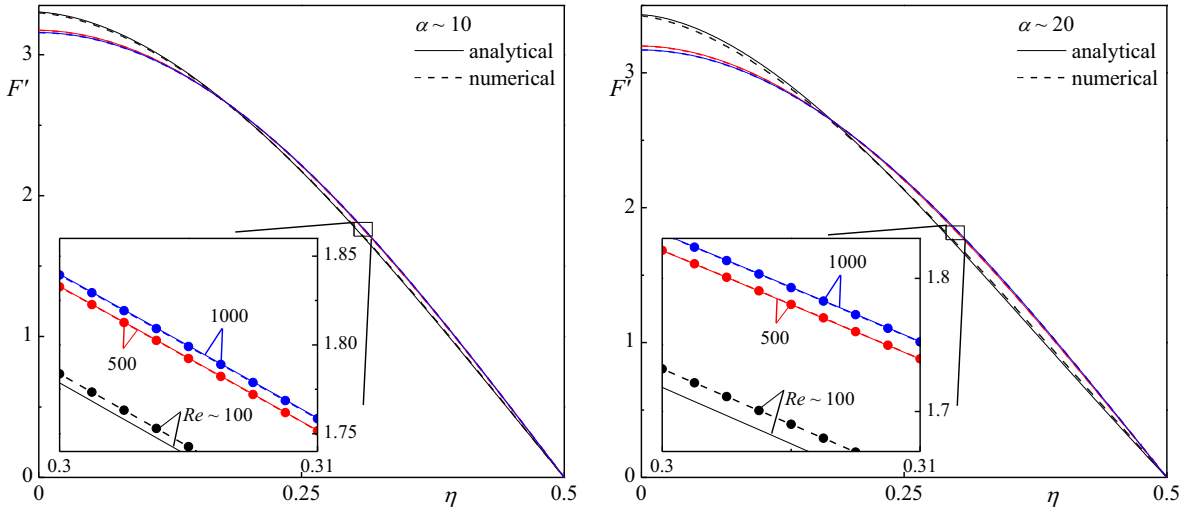

a) $\alpha \approx 10$ **b)** $\alpha \approx 10$

Figure 4. Comparison between analytical (—) and numerical solutions (○) for F' using a) $\alpha \approx 10$, and b) $\alpha \approx 20$. Curves are shown for $Re \approx 100$, 500, and 1000.

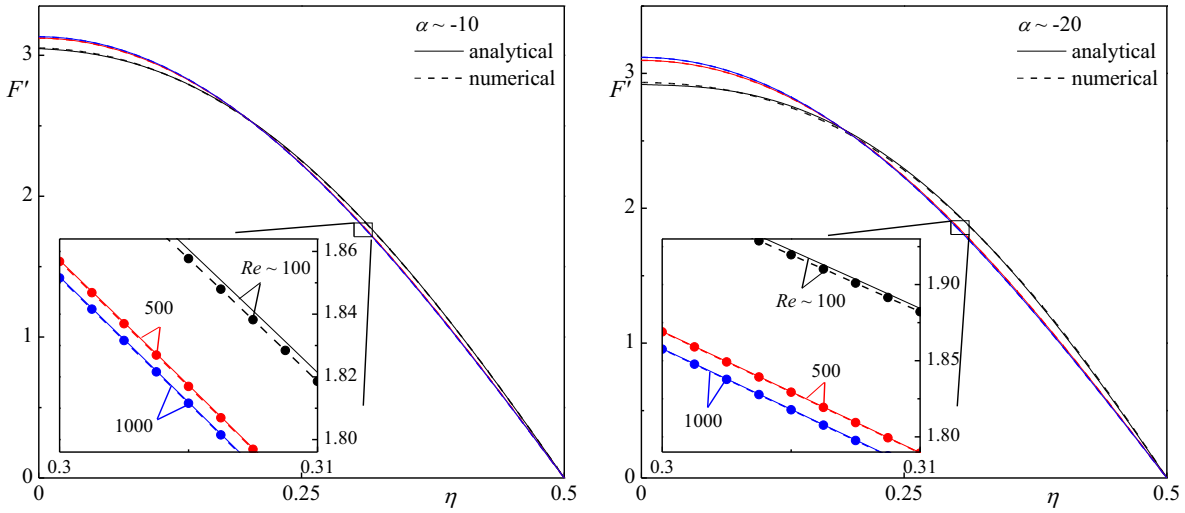

a) $\alpha \approx -10$ **b)** $\alpha \approx -20$

Figure 5. Comparison between analytical (—) and numerical solutions (○) for F' using a) $\alpha \approx -10$, and b) $\alpha \approx -20$. Curves are shown for $Re \approx 100$, 500, and 1000.

or contracting, it may be seen in both tables that the accuracy in F, F' and F'' for the $Re = 1000$ case extends to 4, 3 and 2 significant digits, respectively. A slight degradation in precision occurs as the Reynolds number is lowered first to $Re = 500$, and then to 100. The overall agreement, however, continues to fall approximately within the universally accepted engineering tolerance of 5%.

Given the error entailed in the model itself, the first-order approximation presented here appears to be sufficiently adequate, especially in the modeling of SRM flowfields for which the Reynolds number can be quite large.[24] There might be situations, however, where higher accuracy is desired at intermediate ranges of Re, for example, between 1 and 100. For such cases, higher-order approximations will be required and these could be obtained by resorting to powerful techniques such as perturbation analysis,[67] Lie-group theory,[59,60] Adomian decomposition,[64] or Homotopy Analysis Method (HAM).[61]

Table 1. Comparison between numerical and analytical solutions for the large injection case with $\alpha = 10$ and $Re = 100$, 500, and 1000. Samples are taken at representative radial positions of $\eta = \left\{0, \frac{1}{8}, \frac{1}{4}, \frac{3}{8}, \frac{1}{2}\right\}$

		F		F'		F''	
Re	η	analytical	numerical	analytical	numerical	analytical	numerical
	0	0.0000	0.0000	3.3033	3.2982	-0.3948	-0.6082
	0.125	0.4086	0.3956	3.0032	2.9454	-5.6225	-4.7169
100	0.25	0.7204	0.7192	2.1719	2.1740	-7.4905	-7.4199
	0.375	0.9336	0.9283	1.0706	1.1410	-8.7196	-8.8978
	0.5	1.0000	1.0000	0.0000	0.000004	-9.0731	-9.1578
	0	0.0000	0.0000	3.1739	3.1729	-0.0789	-0.0915
	0.125	0.3854	0.3854	2.9125	2.9114	-3.9774	-3.9728
500	0.25	0.7098	0.7097	2.2115	2.2110	-7.0813	-7.0745
	0.375	0.9248	0.9248	1.1887	1.1886	-9.0728	-9.0684
	0.5	1.0000	1.000	0.0000	0.0000	-9.7100	-9.7087
	0	0.0000	0.0000	3.1577	3.1569	-0.0394	-0.0430
	0.125	0.3840	0.3840	2.9074	2.9066	-3.8772	-3.8746
1000	0.25	0.7084	0.7084	2.2164	2.2159	-7.0301	-7.0256
	0.375	0.9243	0.9243	1.1954	1.1952	-9.0955	-9.0909
	0.5	1.0000	1.0000	0.0000	0.0000	-9.7898	-9.7857

Table 2. Comparison between numerical and analytical solutions for the large injection case with $\alpha = -10$ and $Re = 100$, 500, and 1000. Samples are taken at representative radial positions of $\eta = \left\{0, \frac{1}{8}, \frac{1}{4}, \frac{3}{8}, \frac{1}{2}\right\}$

		F		F'		F''	
Re	η	analytical	numerical	analytical	numerical	analytical	numerical
	0	0.0000	0.0000	3.0474	3.0521	-0.3947	-0.2091
	0.125	0.3723	0.3729	2.8515	2.8515	-3.0926	-3.1597
100	0.25	0.6958	0.6960	2.2532	2.2493	-6.4548	-6.4480
	0.375	0.9191	0.9191	1.2624	1.2617	-9.2333	-9.2008
	0.5	1.0000	1.0000	0.0000	0.0000	-10.6958	-10.7304
	0	0.0000	0.0000	3.1226	3.0521	-0.0789	-0.2091
	0.125	0.3806	0.3806	2.8922	2.8917	-3.6392	-3.6408
500	0.25	0.7048	0.6960	2.2278	2.2493	-6.8735	-6.4480
	0.375	0.9229	0.9229	1.2143	1.2141	-9.1416	-9.1373
	0.5	1.0000	1.000	0.0000	0.0000	-10.0356	-10.7304
	0	0.0000	0.0000	3.1321	3.1316	-0.0394	-0.0353
	0.125	0.3816	0.3816	2.8973	2.8968	-3.7081	-3.7076
1000	0.25	0.7059	0.7059	2.2246	2.2242	-6.9262	-6.9238
	0.375	0.9234	0.9234	1.2082	1.2080	-9.1299	-9.1265
	0.5	1.0000	1.0000	0.0000	0.000007	-9.9525	-9.9496

B. Small Injection/Suction with Low Regression

In this case, both the Reynolds number and the expansion ratio are low. This necessitates rewriting Eq. (37) as

$$2\eta F'''' + \alpha(2\eta F''' + 4F'') + Re(FF''' - F'F'') + 4F''' = 0 \tag{79}$$

To solve Eq. (79) using a perturbation expansion, one needs to expand in both small parameters, Re and α. This is done by setting:

$$F = F_0 + ReF_1 + O(Re^2) \tag{80}$$
$$F_0 = F_{00} + \alpha F_{01} + O(\alpha^2) \tag{81}$$
$$F_1 = F_{10} + \alpha F_{11} + O(\alpha^2) \tag{82}$$

1. Leading-Order Solution

At leading order in Re (i.e. $Re = 0$), we have

$$2\eta F_0'''' + \alpha(2\eta F_0''' + 4F_0'') + 4F_0''' = 0 \tag{83}$$

then given

$$F_0 = F_{00} + \alpha F_{01} + O(\alpha^2) \tag{84}$$

the leading and first-order equations in α may be found to be

$$O(0): \quad \eta F_{00}'''' + 2F_{00}''' = 0 \tag{85a}$$
$$O(\alpha): \quad \eta F_{01}'''' + 2F_{01}''' = -\eta F_{00}''' - 2F_{00}'' \tag{85b}$$

The solution of Eq. (85a) is

$$F_{00} = -4\eta^2 + 4\eta \tag{86}$$

with F_{00} known, Eq. (85b) becomes

$$\eta F_{01}'''' + 2F_{01}''' = 16 \tag{87}$$

Since the boundary conditions are fulfilled by F_{00}, the conditions on all remaining orders must be null. This is implemented by taking

$$\begin{cases} F_{0i}'(\frac{1}{2}) = 0; & F_{0i}(\frac{1}{2}) = 0 \\ F_{0i}(0) = 0; & \lim\limits_{\eta\to 0} \sqrt{2\eta} F_{0i}''(\eta) = 0 \end{cases}; \quad i = 1, 2, 3 \cdots \tag{88}$$

The solution of Eq. (87) becomes

$$F_{01} = \tfrac{1}{3}(4\eta^3 - 4\eta^2 + \eta) \tag{89}$$

Finally, the leading-order solution may be combined into

$$F_0 = F_{00} + \alpha F_{01} = -4\eta^2 + 4\eta + \tfrac{1}{3}\alpha\left(4\eta^3 - 4\eta^2 + \eta\right) \tag{90}$$

2. First-Order Solution

At first order in Re, we have

$$2\eta F_1'''' + \alpha(2\eta F_1''' + 4F_1'') + 4F_1''' = F_0'F_0'' - F_0F_0''' \tag{91}$$

As before, the leading and first-order equations in α may be collected at successive orders such that

$$O(0): \quad \eta F_{10}'''' + 2F_{10}''' = 32\eta - 16 \tag{92a}$$
$$O(\alpha): \quad \eta F_{11}'''' + 2F_{11}''' = -\eta F_{10}''' - 2F_{10}'' + \tfrac{4}{9}(-72\eta^2 + 48\eta - 15) \tag{92b}$$

The corresponding solutions may be expressed as

$$F_{10} = \tfrac{1}{9}(4\eta^4 - 12\eta^3 + 9\eta^2 - 2\eta) \tag{93}$$

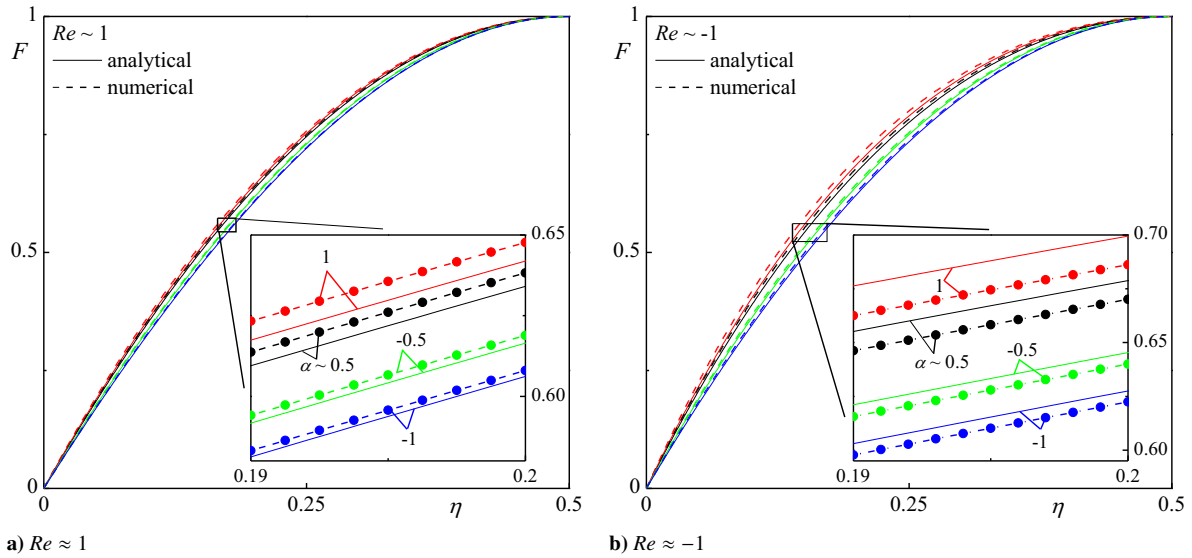

a) $Re \approx 1$ **b)** $Re \approx -1$

Figure 6. Comparison between analytical (—) and numerical solutions (○) for F using (a) $Re \approx 1$, and (b) $Re \approx -1$. Curves are shown for $\alpha \approx 0.5, 1, -0.5,$ and -1.

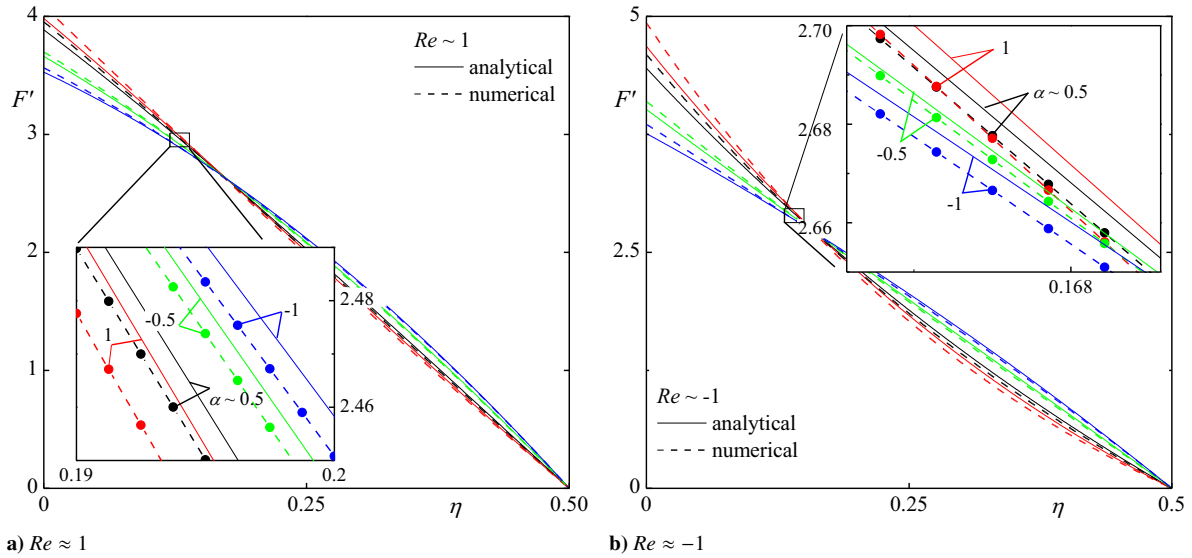

a) $Re \approx 1$ **b)** $Re \approx -1$

Figure 7. Comparison between analytical (—) and numerical solutions (○) for F' using a) $Re \approx 1$, and b) $Re \approx -1$. Curves are shown for $\alpha \approx 0.5, 1, -0.5,$ and -1.

and

$$F_{11} = \tfrac{1}{9}\left(-2\eta^5 + \tfrac{17}{3}\eta^4 - 8\eta^3 + \tfrac{19}{4}\eta^2 - \tfrac{23}{24}\eta\right) \tag{94}$$

The first-order solution is therefore

$$F_1 = \tfrac{1}{9}(4\eta^4 - 4\eta^3 + \eta^2 - 2\eta) + \tfrac{1}{9}\alpha\left(-2\eta^5 + \tfrac{17}{3}\eta^4 - 8\eta^3 + \tfrac{19}{4}\eta^2 - \tfrac{23}{24}\eta\right) \tag{95}$$

3. Verification

The total solution for the small injection case with low regression becomes

$$\begin{aligned} F = &-4\eta(\eta-1) + \tfrac{1}{3}\alpha\,\eta\left(4\eta^2 - 4\eta + 1\right) + \tfrac{1}{9}Re\,\eta(4\eta^3 - 12\eta^2 + 9\eta - 2) \\ &+ \tfrac{1}{9}Re\,\alpha\,\eta\left(-2\eta^4 + \tfrac{17}{3}\eta^3 - 8\eta^2 + \tfrac{19}{4}\eta - \tfrac{23}{24}\right) \end{aligned} \tag{96}$$

Comparisons with numerical solutions are presented in Figs. 6–7 for $Re = \pm 1$ and representative values of $\alpha = -1$, -0.5, 0.5, and 1. In general, the curves corresponding to both analytical and numerical results may be seen to exhibit substantial agreement. As one would expect, the agreement between numerics and asymptotics depreciates with increasing values of the Reynolds number as well as increasing values of the wall expansion ratio. Larger values of the Reynolds number will not be suitable for comparison because of the nature of the perturbation expansion that is based on small values of *Re*.

As before, side-by-side comparisons between numerics and asymptotics are provided in Tables 3 and 4 where approximate representations of F, F' and F'' are showcased against their numerical estimates for two wall expansion ratios of -1 and $+1$, and either $Re = 1$ (Table 3) or -1 (Table 4). For these small injection or suction cases, computed values are given at five radial positions corresponding to $\eta = 0, 0.125, 0.25, 0.375$ and 0.5. Recalling that the asymptotic expansion is carried out in orders of *Re*, it is not surprising that the accuracy of the analytical

Table 3. Comparison between numerical and analytical solutions for the small injection case with $Re \approx 1$ and $\alpha = \pm 1$. Samples are taken at representative radial positions of $\eta = \left\{0, \frac{1}{8}, \frac{1}{4}, \frac{3}{8}, \frac{1}{2}\right\}$

		F		F'		F''	
α	η	analytical	numerical	analytical	numerical	analytical	numerical
	0	0.0000	0.0000	3.5272	3.5636	-4.2168	-4.5987
	0.125	0.4043	0.4064	2.9127	2.9145	-5.6268	-5.8030
-1	0.25	0.7207	0.7221	2.1191	2.1094	-7.0710	-7.0892
	0.375	0.9266	0.9269	1.1459	1.1397	-8.4905	-8.4333
	0.5	1.0000	1.0000	0.0000	0.000002	-9.8265	-9.8035
	0	0.0000	0.0000	3.9824	4.0866	-7.3893	-8.4808
	0.125	0.4382	0.4444	3.0174	3.0254	-7.9807	-8.4651
1	0.25	0.7523	0.7569	2.0034	1.9777	-8.1844	-8.2709
	0.375	0.9389	0.9403	0.9850	0.9637	-8.0588	-7.9303
	0.5	1.0000	1.0000	0.0000	0.000003	-7.6622	-7.4717

Table 4. Comparison between numerical and analytical solutions for the small injection case with $Re \approx -1$ and $\alpha = \pm 1$. Samples are taken at representative radial positions of $\eta = \left\{0, \frac{1}{8}, \frac{1}{4}, \frac{3}{8}, \frac{1}{2}\right\}$

		F		F'		F''	
α	η	analytical	numerical	analytical	numerical	analytical	numerical
	0	0.0000	0.0000	3.7585	3.8565	-6.0736	-7.1347
	0.125	0.4204	0.4261	2.9532	2.9588	-6.8021	-7.2564
-1	0.25	0.7346	0.7386	2.0593	2.0348	-7.4990	-7.5599
	0.375	0.9316	0.9327	1.0773	1.0593	-8.2231	-8.0914
	0.5	1.0000	1.0000	0.0000	0.000003	-9.0332	-8.9109
	0	0.0000	0.0000	4.6831	4.9333	-13.9106	-16.6442
	0.125	0.4836	0.4982	3.1084	3.1252	-11.3508	-12.4811
1	0.25	0.7894	0.8001	1.8301	1.7702	-9.1582	-9.3458
	0.375	0.9517	0.9550	0.8058	0.7565	-7.2776	-6.9838
	0.5	1.0000	1.0000	0.0000	0.000003	-5.6541	-5.2039

approximation is lower than its large injection/suction counterpart, specifically where the perturbation series rather depended on $\epsilon = 1/Re \approx O(10^{-3} - 10^{-2})$; the present $\epsilon \approx 1$ is considerably larger in comparison. In view of this conservative value of $|\epsilon = Re|$, tabulated results reflect diminishing accuracy going from the parent function, F, to its derivatives, F' and F''. Furthermore, it may be seen that higher accuracy is achieved for radial positions corresponding to $\eta \geq \frac{1}{4}$. Those closer to the centerline exhibit lower precision, down to a single digit accuracy, while those closer to the sidewall reflect double or triple digit accuracy.

It should be noted that this solution is not connected with solid rocket propulsion due to the large injection rates that characterize propellant burning. However, it is relevant to other problems involving sweat cooling, filtration, peristaltic pumping, boundary layer control, and so on, where the injection or suction Reynolds number at the slowly moving surface is small. Under special circumstances, it may be suitably used to characterize hybrid motors in which the fuel regression rate is substantially low.

V. Concluding Remarks

This paper revisits the problem of a viscous incompressible fluid in a porous cylinder with an expanding or contracting sidewall. The method that we use is based on conventional, regular perturbation expansions in two distinct physical settings: large injection ($Re \to \infty$), and small injection or suction with weak regression. One of the key aspects of this study stands in the development of a robust numerical algorithm that obviates the need to use predictor-corrector or shooting schemes. At the outset, numerical results are obtained directly, in fact nearly instantaneously, given an assortment of 3 guesses: the first and second derivatives of $G(\xi)$ at the origin, and the control parameter β. Given that $G(0) = 0$ is fixed, we find it best for the cases at hand to set $G'(0) > 0$ and $G''(0) < 0$, and then carefully vary β to the extent of canvassing the solution domain for the desired parameters. For once convergence is achieved, the values of $Re = 2G(\frac{1}{2}b)$ and $\alpha = b\beta$ can be instantly deduced.

In principle, this approach outperforms the technique devised by Dauenhauer and Majdalani,[58] where Re and α are directly specified, although iteration on the initial guesses is still required until convergence is achieved. In actuality, however, both techniques involve some level of iteration, and the ability to prescribe Re and α beforehand remains the main advantage of the Dauenhauer-Majdalani approach, despite its reliance on guesswork and the Newton-Raphson scheme to accelerate convergence.

In the present algorithm, the effort lies in solving as many cases as possible near the desired values of the Reynolds number and wall expansion ratio. Evidently, to minimize labor and eliminate trial-and-error in pursuit of convergence to a desired pair of (Re, α), generating a look-up table in which the practical range of Re and α is finely canvassed would be most efficient. The development of such a look-up table will, however, require a systematic procedure for varying the two initial guesses and β. The procedure described here will be quite suitable in filling the look-up table, given a predefined matrix for initial guesses. But while a look-up table offers numerous advantages, the solutions reported in this article were found manually.

Our numerical simulations were carried out at representative values of the Reynolds number and the wall expansion ratio. It was determined that, so long as the control parameters were chosen from their prescribed asymptotic range, the corresponding analytical approximations and their numerical predictions agreed substantially. In comparison to other series approximations that have since appeared in the literature, the expressions associated with a perturbation expansion remain relatively compact, thus adding physical insight to the problem under investigation. Other series expressions, such as those obtained through the Homotopy-Analysis Method,[61] also offer distinct advantages. These include improved accuracy, controlled convergence to the desired solution (in the case of multiple solutions), and extended ranges of applicability, especially that their precision is incommensurate with the size of Re and α. Their main drawback remains, however, their typical reliance on such a large number of terms to make them nearly equivalent to an elegant numerical routine. As for the asymptotic approximations, they are always more compact and often lead to the identification of key similarity parameters and scales. From an engineering perspective, their accuracy is often sufficient with the retention of only one term beyond the leading-order approximation. In future work, it is hoped that both HAM and perturbation tools will continue to receive attention given their clearly visible benefits and complementary natures.

Acknowledgments

This material is based on work supported partly by the National Science Foundation through Grant No. CMMI-0928762, and partly by the University of Tennessee Space Institute, through institutional cost sharing.

References

[1]Majdalani, J., Vyas, A. B., and Flandro, G. A., "Higher Mean–Flow Approximation for a Solid Rocket Motor with Radially Regressing Walls," *AIAA Journal*, Vol. 40, No. 9, 2002, pp. 1780–1788. doi:10.2514/2.1854.

[2]Majdalani, J., Vyas, A. B., and Flandro, G. A., "Higher Mean–Flow Approximation for a Solid Rocket Motor with Radially Regressing Walls - Erratum," *AIAA Journal*, Vol. 47, No. 1, 2009, pp. 286–286. doi:10.2514/1.40061.

[3]Majdalani, J., and Zhou, C., "Moderate-to-Large Injection and Suction Driven Channel Flows with Expanding or Contracting Walls," *Journal of Applied Mathematics and Mechanics*, Vol. 83, No. 3, 2003, pp. 181–196. doi:10.1002/zamm.200310018.

[4]Majdalani, J., and Akiki, M., "Rotational and Quasiviscous Cold Flow Models for Axisymmetric Hybrid Propellant Chambers," *Journal of Fluids Engineering*, Vol. 132, No. 10, 2010, pp. 101202–7. doi:10.1115/1.4002397.

[5]Majdalani, J., "Analytical Models for Hybrid Rockets," *Fundamentals of Hybrid Rocket Combustion and Propulsion*, edited by K. Kuo and M. J. Chiaverini, Progress in Astronautics and Aeronautics, chap. Chap. 5, AIAA Progress in Astronautics and Aeronautics, Washington, DC, 2007, pp. 207–246.

[6]Peng, Y., and Yuan, S. W., "Laminar Pipe Flow with Mass Transfer Cooling," *Journal of Heat Transfer*, Vol. 87, No. 2, May 1965, pp. 252–258.

[7]Yuan, S. W., and Finkelstein, A. B., "Heat Transfer in Laminar Pipe Flow with Uniform Coolant Injection," *Jet Propulsion*, Vol. 28, No. 1, 1958, pp. 178–181.

[8]Acrivos, A., "The Asymptotic Form of the Laminar Boundary-Layer Mass-Transfer Rate for Large Interfacial Velocities," *Journal of Fluid Mechanics*, Vol. 12, No. 3, 1962, pp. 337–357. doi:10.1017/S0022112062000257.

[9]Libby, P. A., "The Homogeneous Boundary Layer at an Axisymmetric Stagnation Point with Large Rates of Injection," *Journal of the Aerospace Sciences*, Vol. 29, No. 1, 1962, pp. 48–60.

[10]Libby, P. A., and Pierucci, M., "Laminar Boundary Layer with Hydrogen Injection Including Multicomponent Diffusion," *AIAA Journal*, Vol. 2, No. 12, December 1964, pp. 2118–2126. doi:10.2514/3.2752.

[11]Fung, Y. C., and Yih, C. S., "Peristaltic Transport," *Journal of Applied Mechanics*, Vol. 35, No. 4, December 1968, pp. 669–675.

[12]Uchida, S., and Aoki, H., "Unsteady Flows in a Semi–Infinite Contracting or Expanding Pipe," *Journal of Fluid Mechanics*, Vol. 82, No. 2, 1977, pp. 371–387. doi:10.1017/S0022112077000718.

[13]Berman, A. S., "Laminar Flow in Channels with Porous Walls," *Journal of Applied Physics*, Vol. 24, No. 9, 1953, pp. 1232–1235. doi:10.1063/1.1721476.

[14]Berman, A. S., "Effects of Porous Boundaries on the Flow of Fluids in Systems with Various Geometries," *Proceedings of the Second United Nations International Conference on the Peaceful Uses of Atomic Energy*, Vol. 4, 1958, pp. 351–358.

[15]Berman, A. S., "Laminar Flow in an Annulus with Porous Walls," *Journal of Applied Physics*, Vol. 29, No. 1, 1958, pp. 71–75. doi:10.1063/1.1722948.

[16]Yuan, S. W., and Finkelstein, A. B., "Laminar Pipe Flow with Injection and Suction through a Porous Wall," *Transactions of the American Society of Mechanical Engineers: Journal of Applied Mechanics*, Vol. 78, No. 3, May 1956, pp. 719–724.

[17]Terrill, R. M., and Thomas, P. W., "On Laminar Flow Through a Uniformly Porous Pipe," *Applied Scientific Research*, Vol. 21, No. 1, 1969, pp. 37–67. doi:10.1007/BF00411596.

[18]Terrill, R. M., "On Some Exponentially Small Terms Arising in Flow through a Porous Pipe," *Quarterly Journal of Mechanics and Applied Mathematics*, Vol. 26, No. 3, 1973, pp. 347–354. doi:10.1093/qjmam/26.3.347.

[19]Terrill, R., "Laminar Flow in a Porous Tube," *ASME Journal of Fluids Engineering*, Vol. 105, No. 3, 1983, pp. 303–307. doi:10.1115/1.3240992.

[20]Skalak, F. M., and Wang, C.-Y., "On the Nonunique Solutions of Laminar Flow through a Porous Tube or Channel," *SIAM Journal on Applied Mathematics*, Vol. 34, No. 3, May 1978, pp. 535–544. doi:10.1137/0134042.

[21]Taylor, G. I., "Fluid Flow in Regions Bounded by Porous Surfaces," *Proceedings of the Royal Society of London, Series A*, Vol. 234, No. 1199, March 1956, pp. 456–475. doi:10.1098/rspa.1956.0050.

[22]Culick, F. E. C., "Rotational Axisymmetric Mean Flow and Damping of Acoustic Waves in a Solid Propellant Rocket," *AIAA Journal*, Vol. 4, No. 8, 1966, pp. 1462–1464. doi:10.2514/3.3709.

[23]Casalis, G., Avalon, G., and Pineau, J.-P., "Spatial Instability of Planar Channel Flow with Fluid Injection through Porous Walls," *Physics of Fluids*, Vol. 10, No. 10, 1998, pp. 2558–2568. doi:10.1063/1.869770.

[24]Chedevergne, F., Casalis, G., and Féraille, T., "Biglobal Linear Stability Analysis of the Flow Induced by Wall Injection," *Physics of Fluids*, Vol. 18, No. 1, 2006, pp. 014103–14. doi:10.1063/1.2160524.

[25]Griffond, J., and Casalis, G., "On the Dependence on the Formulation of Some Nonparallel Stability Approaches Applied to the Taylor Flow," *Physics of Fluids*, Vol. 12, No. 2, February 2000, pp. 466–468. doi:10.1063/1.870323.

[26]Griffond, J., and Casalis, G., "On the Nonparallel Stability of the Injection Induced Two-Dimensional Taylor Flow," *Physics of Fluids*, Vol. 13, No. 6, June 2001, pp. 1635–1644. doi:10.1063/1.1367869.

[27]Griffond, J., Casalis, G., and Pineau, J.-P., "Spatial Instability of Flow in a Semiinfinite Cylinder with Fluid Injection through Its Porous Walls," *European Journal of Mechanics B/Fluids*, Vol. 19, No. 1, 2000, pp. 69–87. doi:10.1016/S0997-7546(00)00105-9.

[28]Abu-Irshaid, E. M., Majdalani, J., and Casalis, G., "Hydrodynamic Stability of Rockets with Headwall Injection," *Physics of Fluids*, Vol. 19, No. 2, 2007, pp. 024101–11. doi:10.1063/1.2434797.

[29]Majdalani, J., Flandro, G. A., and Roh, T. S., "Convergence of Two Flowfield Models Predicting a Destabilizing Agent in Rocket Combustion," *Journal of Propulsion and Power*, Vol. 16, No. 3, 2000, pp. 492–497. doi:10.2514/2.5595.

[30]Fabignon, Y., Dupays, J., Avalon, G., Vuillot, F., Lupoglazoff, N., Casalis, G., and Prévost, M., "Instabilities and Pressure Oscillations in Solid Rocket Motors," *Journal of Aerospace Science and Technology*, Vol. 7, No. 3, April 2003, pp. 191–200. doi:10.1016/S1270-9638(02)01194-X.

[31]Flandro, G. A., and Majdalani, J., "Aeroacoustic Instability in Rockets," *AIAA Journal*, Vol. 41, No. 3, February 2003, pp. 485–497. doi:10.2514/2.1971.

[32]Majdalani, J., Flandro, G. A., and Fischbach, S. R., "Some Rotational Corrections to the Acoustic Energy Equation in Injection-Driven Enclosures," *Physics of Fluids*, Vol. 17, No. 7, 2005, pp. 0741021–20. doi:10.1063/1.1920647.

[33]Majdalani, J., Fischbach, S. R., and Flandro, G. A., "Improved Energy Normalization Function in Rocket Motor Stability Calculations," *Journal of Aerospace Science and Technology*, Vol. 10, No. 6, September 2006, pp. 495–500. doi:10.1016/j.ast.2006.06.002.

[34]Flandro, G. A., Fischbach, S. R., and Majdalani, J., "Nonlinear Rocket Motor Stability Prediction: Limit Amplitude, Triggering, and Mean Pressure Shift," *Physics of Fluids*, Vol. 19, No. 9, September 2007, pp. 094101–16. doi:10.1063/1.2746042.

[35]Fischbach, S. R., Majdalani, J., and Flandro, G. A., "Acoustic Instability of the Slab Rocket Motor," *Journal of Propulsion and Power*, Vol. 23, No. 1, January-February 2007, pp. 146–157. doi:10.2514/1.14794.

[36]Majdalani, J., and Roh, T., "The Oscillatory Channel Flow with Large Wall Injection," *Proceedings of the Royal Society of London, Series A*, Vol. 456, No. 1999, July 2000, pp. 1625–1657. doi:10.1098/rspa.2000.0579.

[37]Majdalani, J., "The Oscillatory Channel Flow with Arbitrary Wall Injection," *Journal of Applied Mathematics and Physics (ZAMP)*, Vol. 52, No. 1, 2001, pp. 33–61. doi:10.1007/PL00001539.

[38]Majdalani, J., and Flandro, G. A., "The Oscillatory Pipe Flow with Arbitrary Wall Injection," *Proceedings of the Royal Society of London, Series A*, Vol. 458, No. 2023, July 2002, pp. 1621–1651. doi:10.1098/rspa.2001.0930.

[39]Majdalani, J., "Multiple Asymptotic Solutions for Axially Travelling Waves in Porous Channels," *Journal of Fluid Mechanics*, Vol. 636, No. 1, October 2009, pp. 59–89. doi:10.1017/S0022112009007939.

[40]Féraille, T., and Casalis, G., "Channel Flow Induced by Wall Injection of Fluid and Particles," *Physics of Fluids*, Vol. 15, No. 2, February 2003, pp. 348–360. doi:10.1063/1.1530158.

[41]Clayton, C. D., "Flow fields in Solid Rocket Motors with Tapered Bores," *32nd AIAA/ASME/SAE/ASEE Joint Propulsion Conference*, AIAA Paper 96-2643, Lake Buena Vista, FL, July 1996.

[42]Saad, T., Sams, O. C., and Majdalani, J., "Rotational Flow in Tapered Slab Rocket Motors," *Physics of Fluids*, Vol. 18, No. 1, 2006, pp. 103601–13. doi:10.1063/1.2354193.

[43]Sams, O. C., Majdalani, J., and Saad, T., "Mean Flow Approximations for Solid Rocket Motors with Tapered Walls," *Journal of Propulsion and Power*, Vol. 23, No. 2, March-April 2007, pp. 445–456. doi:10.2514/1.15831.

[44]Sabnis, J. S., Gibeling, H. J., and McDonald, H., "Navier-Stokes Analysis of Solid Propellant Rocket Motor Internal Flows," *Journal of Propulsion and Power*, Vol. 5, No. 6, 1989, pp. 657–664. doi:10.2514/3.23203.

[45]Dunlap, R., Willoughby, P. G., and Hermsen, R. W., "Flowfield in the Combustion Chamber of a Solid Propellant Rocket Motor," *AIAA Journal*, Vol. 12, No. 10, 1974, pp. 1440–1445. doi:10.2514/3.49513.

[46]Dunlap, R., Blackner, A. M., Waugh, R. C., Brown, R. S., and Willoughby, P. G., "Internal Flow Field Studies in a Simulated Cylindrical Port Rocket Chamber," *Journal of Propulsion and Power*, Vol. 6, No. 6, 1990, pp. 690–704. doi:10.2514/3.23274.

[47]Kurdyumov, V. N., "Steady Flows in the Slender, Noncircular, Combustion Chambers of Solid Propellants Rockets," *AIAA Journal*, Vol. 44, No. 12, December 2006, pp. 2979–2986. doi:10.2514/1.21125.

[48]Majdalani, J., and Saad, T., "The Taylor-Culick Profile with Arbitrary Headwall Injection," *Physics of Fluids*, Vol. 19, No. 9, September 2007, pp. 093601–10. doi:10.1063/1.2746003.

[49]Saad, T., and Majdalani, J., "On the Lagrangian Optimization of Wall-Injected Flows: From the Hart-McClure Potential to the Taylor-Culick Rotational Motion," *Proceedings of the Royal Society of London, Series A*, Vol. 466, No. 2114, February 2010, pp. 331–362. doi:10.1098/rspa.2009.0326.

[50]Hart, R. W., and McClure, F. T., "Combustion Instability: Acoustic Interaction with a Burning Propellant Surface," *The Journal of Chemical Physics*, Vol. 30, No. 6, June 1959, pp. 1501–1514. doi:10.1063/1.1730226.

[51]McClure, F., Hart, R., and Cantrell, R., "Interaction between Sound and Flow: Stability of T-Burners," *AIAA Journal*, Vol. 1, No. 3, 1963, pp. 586–590. doi:10.2514/3.54846.

[52]McClure, F. T., Hart, R. W., and Bird, J. F., "Acoustic Resonance in Solid Propellant Rockets," *Journal of Applied Physics*, Vol. 31, No. 5, May 1960, pp. 884–896. doi:10.1063/1.1735713.

[53]Cantrell, R. H., Hart, R. W., and McClure, F. T., "Acoustic Energy Losses in Rocket-Engine Cavities," *Journal of the Acoustical Society of America*, Vol. 35, No. 5, 1963, pp. 773–773. doi:10.1121/1.2142356.

[54]Hart, R. W., Bird, J. F., Cantrell, R. H., and McClure, F. T., "Nonlinear Effects in Instability of Solid Propellant Rocket Motors," *AIAA Journal*, Vol. 2, No. 7, 1964, pp. 1270–1273. doi:10.2514/3.55069.

[55]Goto, M., and Uchida, S., "Unsteady Flows in a Semi–Infinite Expanding Pipe with Injection Through Wall," *Journal of the Japan Society for Aeronautical and Space Sciences*, Vol. 38, 1990, pp. 434.

[56]Dauenhauer, E. C., and Majdalani, J., "Unsteady Flows in Semi-Infinite Expanding Channels with Wall Injection," *30th AIAA Fluid Dynamics Conference*, AIAA Paper 99-3523, Norfolk, VA, June-July 1999.

[57]Dauenhauer, E. C., and Majdalani, J., "Exact Self-Similarity Solution of the Navier-Stokes Equations for a Deformable Channel with Wall Suction or Injection," *37th AIAA/ASME/SAE/ASEE Joint Propulsion Conference and Exhibit*, AIAA Paper 2001-3588, Salt Lake City, UT, July 2001.

[58]Dauenhauer, E. C., and Majdalani, J., "Exact Self-Similarity Solution of the Navier–Stokes Equations for a Porous Channel with Orthogonally Moving Walls," *Physics of Fluids*, Vol. 15, No. 6, 2003, pp. 1485–1495. doi:10.1063/1.1567719.

[59]Boutros, Y. Z., Abd-el Malek, M. B., Badran, N. A., and Hassan, H. S., "Lie-Group Method for Unsteady Flows in a Semi-Infinite Expanding or Contracting Pipe with Injection or Suction through a Porous Wall," *Journal of Computational and Applied Mathematics*, Vol. 197, No. 2, 2006, pp. 465–494. doi:10.1016/j.cam.2005.11.031.

[60]Boutros, Y. Z., Abd-el Malek, M. B., Badran, N. A., and Hassan, H. S., "Lie-Group Method Solution for Two-Dimensional Viscous Flow between Slowly Expanding or Contracting Walls with Weak Permeability," *Applied Mathematical Modelling*, Vol. 31, No. 6, 2007, pp. 1092–1108. doi:10.1016/j.apm.2006.03.026.

[61]Xu, H., Lin, Z.-L., Liao, S.-J., Wu, J.-Z., and Majdalani, J., "Homotopy Based Solutions of the Navier-Stokes Equations for a Porous Channel with Orthogonally Moving Walls," *Physics of Fluids*, Vol. 22, No. 5, May 2010, pp. 05360101–05360118. doi:10.1063/1.3392770.

[62]Dinarvand, S., Rashidi, M., and Doosthoseini, A., "Analytical Approximate Solutions for Two-Dimensional Viscous Flow through Expanding or Contracting Gaps with Permeable Walls," *Central European Journal of Physics*, Vol. 7, No. 4, 2009, pp. 791–799. doi:10.2478/s11534-009-0024-x.

[63]Dinarvand, S., and Rashidi, M. M., "A reliable treatment of a homotopy analysis method for two-dimensional viscous flow in a rectangular domain bounded by two moving porous walls," *Nonlinear Analysis: Real World Applications*, Vol. 11, No. 3, 2010, pp. 1502 – 1512. doi:10.1016/j.nonrwa.2009.03.006.

[64]Liao, S., *Beyond Perturbation: Introduction to the Homotopy Analysis Method*, Chapman & Hall/CRC Press, Boca Raton, FL, 1st ed., 2003.

[65]Liao, S., "On the Homotopy Analysis Method for Nonlinear Problems," *Applied Mathematics and Computation*, Vol. 147, No. 2, January 2004, pp. 499–513. doi:10.1016/S0096-3003(02)00790-7.

[66]Liao, S., and Tan, Y., "A General Approach to Obtain Series Solutions of Nonlinear Differential Equations," *Studies in Applied Mathematics*, Vol. 119, No. 4, October 2007, pp. 297–354. doi:10.1111/j.1467-9590.2007.00387.x.

[67]Maicke, B. A., and Majdalani, J., "On the Rotational Compressible Taylor Flow in Injection-Driven Porous Chambers," *Journal of Fluid Mechanics*, Vol. 603, No. 1, May 2008, pp. 391–411. doi:10.1017/S0022112008001121.